IEEE Robotics and Automation Letters (RA-L) paper, presented at ICRA 2026, Vienna, Austria. Cite as RA-L paper.

Analytical and Computational Modeling of a Stop-Rotor Aircraft with Experimental Validation

Kristan M. Hilby and Ian W. Hunter

***Abstract*—Stop-rotor aircraft are a class of vertical takeoff and landing (VTOL) vehicle that offer improved efficiency across flight modes through the usage of a single central lifting surface. In VTOL, the central lifting surface rotates like a helicopter blade to achieve an upward force. In forward flight, the central lifting surface locks in place like a conventional fixed-wing aircraft and achieves lift from airflow over the surface. The improved efficiency across flight modes enables more complex mission profiles that balance flight time in VTOL and forward flight, such as package delivery and inspection over a large area. Despite the promise of stop-rotor aircraft, challenges in modeling and control, particularly due to the nonlinear rotor dynamics across flight modes, have limited practical implementation. To this end, this paper presents two types of models: 1. Analytical models, derived from first principles physics, provide insight into the stability and control of the vehicle and demonstrate closed-loop stability of yaw and altitude using classical PID control, 2. Computational models, based on numerical integration of the system's ordinary differential equations, provide full-state dynamics of the vehicle. Validation against bench-top constrained flight tests shows that the analytical models capture over 97% of the variance in the computational results, while the computational models account for up to 40% of the variance observed in experimental data.**

***Index Terms*—Dynamics, Aerial Systems, Mechanics and Control**

I. Introduction

VERTICAL takeoff and landing (VTOL) uncrewed aerial vehicles (UAVs) offer distinct advantages for operations in remote or undeveloped areas, providing improved safety, versatility, and agility [1]. Traditional VTOL UAV configurations include tiltrotors with rotating nacelles [2], [3], [4]; tiltwings, where entire wing assemblies rotate [5], [6], [7]; multi-copters (e.g., quadcopters) [8]; and tailsitters that take off and land vertically with the tail on ground and the nose pointed directly upward [9], [10], [11]. While these designs enable VTOL capabilities, they typically compromise efficiency in one flight mode [12], [13], [14]. As mission profiles increasingly require balanced VTOL and cruise performance—such as search and rescue, parcel delivery, and large-scale inspection tasks—efficiency across both flight regimes becomes crucial [15].

Manuscript received: June, 27, 2025; Revised September, 22, 2025; Accepted October, 24, 2025.

This paper was recommended for publication by Soon-Jo Chung upon evaluation of the Reviewers' comments. This work was supported by the MIT Office of Graduate Engineering Zakhartchenko Fellowship.

Both authors are with the Mechanical Engineering Department at the Massachusetts Institute of Technology, Cambridge, MA 02139 USA kmhilby@mit.edu

Digital Object Identifier (DOI): see top of this page.

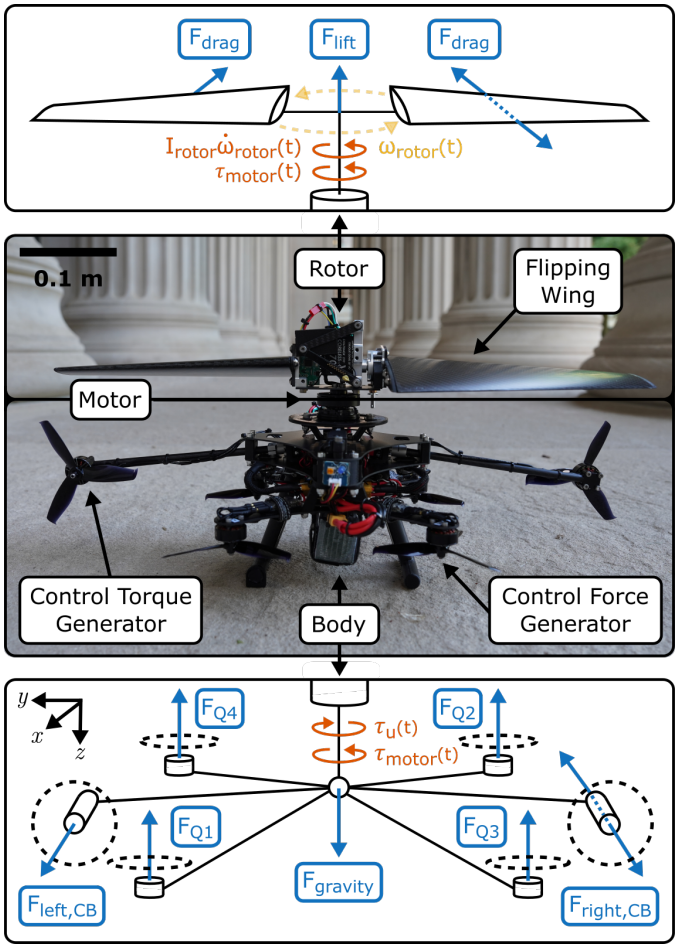

Fig. 1. Overview of the stop-rotor aircraft configuration and its correspondence to the analytical model. The middle panel shows the experimental vehicle with labeled components: rotor and flipping wing, motor, body, control torque generator, and control force generator. The top panel illustrates the simplified analytical model of the rotor assembly, including lift (F_{lift}), drag (F_{drag}), rotor torque ($I_{\text{rotor}}\dot{\omega}_{\text{rotor}}(t)$) due to acceleration, and motor torque ($\tau_{\text{motor}}(t)$). The bottom panel illustrates the analytical representation of the body assembly, with forces (F_{q1}–F_{q4}, F_{gravity}, $F_{\text{left,CB}}$, $F_{\text{right,CB}}$) and torques ($\tau_{\text{u}}(t)$, $\tau_{\text{motor}}(t)$). Together, these panels introduce the physical vehicle and show how its components are abstracted in the analytical model.

Towards this end, stop-rotor aircraft have long been considered a promising VTOL configuration, leveraging a dual-purpose central lifting surface that operates as a helicopter rotor in VTOL and as a fixed wing in forward flight [16],[17], enabling higher cruise and VTOL efficiency without sacrificing capabilities. Despite several prototypes [18], [19], [20], [21], stop-rotor architectures remain largely unexplored due to the complex mechanical design, dynamics, and controls.

One prior configuration, the stopped-penta-rotor (SPERO)

IEEE Robotics and Automation Letters (RA-L) paper, presented at ICRA 2026, Vienna, Austria. Cite as RA-L paper.

[22], demonstrates a mechanically viable architecture validated through real world bidirectional flight tests. While that work validated the platform, the modeling was limited to basic first principles needed to formulate the control system and lacked full six degree of freedom (6-DoF) modeling. Other modeling efforts for stop-rotor aircraft have largely focused on hover-state approximations for simplified co-axial designs [23]. He et al. developed a full state analytical model of a canard rotor wing configuration [24] that advanced simulation-based capabilities, but it was not validated against a physical system and did not address stability, leaving open questions for the practical deployment.

While several prototypes and modeling studies have been reported, systematic stability analysis and experimental validation of stop-rotor architectures are still lacking. These two steps are critical for advancing understanding and enabling deployment of stop-rotor aircraft. To address this gap, this work makes three contributions:

1) **Open loop stability analysis**: Extension of prior first principles analytical models introduced in [22] through open-loop stability characterization.
2) **6-DoF computational model**: Development of a computational model of a stop-rotor aircraft enabling full-state simulation of coupled forces, reconfigurations, and transitions across VTOL, forward flight, and intermediate modes.
3) **Model validation**: Demonstration of consistency between analytical and computational models, and validation of computational predictions against constrained flight experiments.

The remainder of this paper is organized as follows. Section II overviews the vehicle architecture. Section III develops the analytical model, and Section IV presents the computational Simscape model. Section V reports simulation and experimental validation. Section VI discusses model quality and stability insights, and Section VII concludes.

II. Background on System Architecture

The SPERO platform, introduced in [22], serves as the experimental basis for the presented analytical, computational, and validation studies. We summarize only the architectural features relevant to modeling and stability analysis, while referring the reader to [22] for a complete discussion of design, control, and flight validation. Fig. 1 and Fig. 2 illustrate the platform, free-body diagram, and mode-dependent configurations. Component labels (B1–B7 for brushless motors and S1–S3 for servo motors) are used consistently throughout this section.

A. System Overview

SPERO comprises four main actuator groups: a central rotor (B1) with a flipping wing actuated by servo S3, two counterbalance motors (B2–B3) redirected by servos S1 and S2, and four base-mounted vertical-thrust motors (B4–B7). The rotor provides primary lift during VTOL and is mechanically locked in forward flight, while the flipping wing ensures the correct leading-edge orientation across modes. The counterbalances and base motors support yaw control, propulsion, and transition maneuvers depending on the flight state.

B. Flight Mode Dependent Configuration

The actuator groups are employed differently across flight modes. In VTOL, the rotor spins to generate lift, the wing presents opposite leading edges, and the counterbalances generate a net yaw torque $\tau_u(t)$. During transition, servos reorient the counterbalances and flip the wing while the base motors supply vertical force $F_u(t)$. In forward flight, the rotor is locked, the wing aligns on one side, and the counterbalances produce propulsive thrust. These mode-dependent configurations are summarized in Fig. 2 and define the actuator–control mappings used in the analytical model of Section III.

III. Analytical Modeling and Stability Analysis

To study the fundamental dynamics of the stop-rotor configuration, we extend the first-principles model of SPERO [22] into a state-space framework for equilibrium and stability analysis. The section proceeds by summarizing the governing equations, formulating them in nonlinear state space, computing representative equilibria and their linearizations, and analyzing the resulting open-loop stability properties.

A. Model Overview

Analytical modeling focuses on yaw and altitude because these axes are most strongly influenced by the rotor dynamics. Roll and pitch are largely constrained by the symmetry of the design, and are therefore excluded. We adopt the analytical

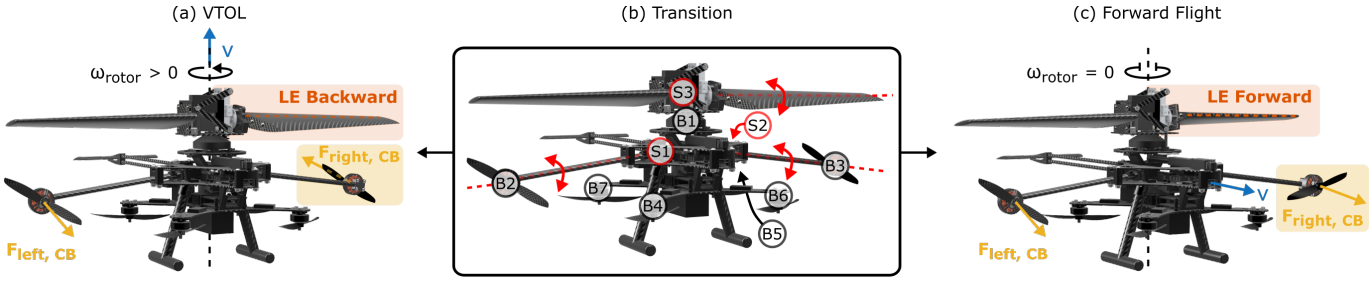

Fig. 2. Overview of the flight modes, transition mechanisms, and motors present in SPERO. In (a) VTOL mode, the main motor (B1) spins the wing with positive angular velocity, ω_{rotor}, which produces a net upward vertical velocity, v. (b) In the transition phase, servos (S1 – S3) actuate to flip the wing and counterbalance (B2 and B3) direction, while additional bottom mounted brushless motors (B4 – B7) provide additional thrust. (c) In forward flight, the main rotor is locked with $\omega_{\text{rotor}} = 0$ and the leading edge (LE) of the flipping wing is facing forward.

IEEE Robotics and Automation Letters (RA-L) paper, presented at ICRA 2026, Vienna, Austria. Cite as RA-L paper.

TABLE I
MAPPING OF MODELED INPUTS AND STATES TO PHYSICAL ACTUATORS

Variable	Symbol	Actuator(s)
Control Torque	τ_u	B2 and S1: Servo-mounted brushless motors
		B3 and S2: Servo-mounted brushless motors
Control Force	F_u	B4 – B7: Base-mounted brushless motors
Rotor Speed	ω_{rotor}	B1: Main rotor motor
Motor Torque	τ_{motor}	B1: Main rotor motor

yaw and altitude models of SPERO derived in [22], extending them by treating rotor speed as a dynamic state and motor torque as the input. This modification enables equilibrium analysis and linearization about steady trim conditions. The model captures the dominant couplings between rotor speed, yaw motion, and altitude under assumptions of decoupled forces, near-axial inflow and rigid-body symmetry.

Table I summarizes the mapping between the modeled forces and torques shown in Fig. 1 and the actuators shown in Fig. 2. Applying Newton's second law to the relationships illustrated in Fig. 1 yields the following equations of motion:

$$I_{\text{rotor}}\ddot{\alpha}_{\text{rotor}}(t) = \tau_{\text{motor}}(t) - \frac{1}{2}\rho c_d A_{\text{ref}} r^3 \omega_{\text{rotor}}(t)^2, \quad (1)$$

$$I_{\text{body}}\ddot{\alpha}_{\text{body}}(t) = -\tau_{\text{motor}}(t) + \tau_{\text{u}}(t), \quad (2)$$

$$m\ddot{z}(t) = mg - \tfrac{1}{2}\rho c_l A_{\text{ref}} r^2 \omega_{\text{rotor}}(t)^2 - F_{\text{u}}(t), \quad (3)$$

where t is time; I_{body} and I_{rotor} are the moments of inertia of the body and rotor, respectively; $\ddot{\alpha}_{\text{body}}(t)$ and $\ddot{\alpha}_{\text{rotor}}(t)$ are the angular acceleration of the body and rotor, respectively; τ_{motor} is the torque introduced by the main motor (B1), which is spinning with angular speed $\omega_{\text{rotor}}(t)$; ρ is air density; c_d and c_l are the drag and lift coefficient of the wing, respectively; A_{ref} is the wing reference area; r is the distance between the axis of rotation and the wing center of pressure; $\tau_{\text{u}}(t)$ is a control torque supplied by the thrust vectored counterbalances (B2 and B3, oriented with S1 and S2); $z(t)$ is the vehicle's altitude; m is the body mass; g is the gravitational constant; and $F_{\text{u}}(t)$ is the control force supplied by the base mounted motors (B4 – B7).

B. Nonlinear State-Space Formulation

To enable stability analysis, Equations 1 – 3 are cast into a nonlinear state-space representation with the states and inputs defined as

$$\mathbf{x}(t) = \begin{bmatrix} x_1(t) \\ x_2(t) \\ x_3(t) \end{bmatrix} = \begin{bmatrix} \omega_{\text{rotor}}(t) \\ \omega_{\text{body}}(t) \\ \dot{z}(t) \end{bmatrix},$$

$$\mathbf{u}(t) = \begin{bmatrix} u_1(t) \\ u_2(t) \\ u_3(t) \end{bmatrix} = \begin{bmatrix} \tau_{\text{motor}}(t) \\ \tau_u(t) \\ F_u(t) \end{bmatrix}.$$

The nonlinear dynamics (i.e., Equations 1 – 3) are then expressed as

$$\dot{\mathbf{x}} = f(\mathbf{x}, \mathbf{u}) = \begin{bmatrix} \dfrac{u_1 - K_d x_1^2}{I_{\text{rotor}}} \\ \dfrac{-u_1 + u_2}{I_{\text{body}}} \\ g - \dfrac{K_\ell x_1^2 + u_3}{m} \end{bmatrix}, \quad (4)$$

where $K_d = \frac{1}{2}\rho c_d A_{\text{ref}} r^3$ and $K_\ell = \frac{1}{2}\rho c_l A_{\text{ref}} r^2$.

C. Linearization and Stability Analysis

The state space model (Equation 4) captures the nonlinear and coupled influence of rotor speed across the states; however, the stability of the system is difficult to interpret directly from Equation 4. Therefore, to gain insight into system stability, we examine three cases of practical interest: Case I (rotor at rest) represents the stop-rotor condition during transition, when the vehicle relies on aerodynamic lift and control authority is most limited. Case II (constant rotor speed) corresponds to nominal VTOL operation, where rotor speed provides steady lift and altitude control. Case III (constant rotor acceleration) captures the dynamics during rotor spin-up or spin-down transition between Case I and Case II. Case I and Case II define equilibrium trim points of the system, while Case III corresponds to a time-varying trajectory. Linearization about these conditions, as well as their open-loop stability implications, are reviewed below.

1) Equilibrium Points

Equilibria are time-invariant operating conditions $(\mathbf{x}^*, \mathbf{u}^*)$ satisfying

$$\dot{\mathbf{x}}(t) = f(\mathbf{x}(t), \mathbf{u}(t)) = \mathbf{0} \quad \Rightarrow \quad f(\mathbf{x}^*, \mathbf{u}^*) = \mathbf{0},$$

i.e., $\mathbf{x}^*(t) \equiv \mathbf{x}^*$ and $\mathbf{u}^*(t) \equiv \mathbf{u}^*$ are constant in time. From Equation 4, it follows that

$$u_1^* = K_d (x_1^*)^2, \qquad u_2^* = u_1^*, \qquad u_3^* = mg - K_\ell (x_1^*)^2.$$

We consider two equilibrium trims resulting from Case I ($x_1^* = 0$) and Case II ($x_1^* = \omega > 0$). Linearization about $(\mathbf{x}^*, \mathbf{u}^*)$ yields the time-invariant perturbation model $\delta\dot{\mathbf{x}}(t) = A\,\delta\mathbf{x}(t) + B\,\delta\mathbf{u}(t)$, with Jacobians

$$A = \begin{bmatrix} -\frac{2K_d x_1^*}{I_{\text{rotor}}} & 0 & 0 \\ 0 & 0 & 0 \\ -\frac{2K_\ell x_1^*}{m} & 0 & 0 \end{bmatrix}, \quad (5)$$

$$B = \begin{bmatrix} \dfrac{1}{I_{\text{rotor}}} & 0 & 0 \\ -\dfrac{1}{I_{\text{body}}} & \dfrac{1}{I_{\text{body}}} & 0 \\ 0 & 0 & -\dfrac{1}{m} \end{bmatrix}. \quad (6)$$

The eigenvalues of A characterize open-loop stability:

$$\lambda(A) = \{\, 0,\ 0,\ -2K_d x_1^* / I_{\text{rotor}} \,\}.$$

For Case I, all poles are at the origin (i.e., three integrators), whereas for Case II the rotor channel contributes a stable pole with time constant $\tau_{\text{rotor}} = I_{\text{rotor}}/(2K_d\omega)$ while yaw and altitude remain integrators (i.e., two integrators). Both Case I and Case II present marginally stable open-loop dynamics, requiring feedback control to ensure stable operation.

2) Time-Varying Trajectory

For rotor spin up and down we consider a time-varying operating point $\mathbf{x}^\star(t)$ with $x_1^\star(t) = \omega_{\text{rotor}}^\star(t) = at$, $x_2^\star(t) = 0$, $x_3^\star(t) = 0$, and corresponding inputs $\mathbf{u}^\star(t)$ satisfying $f(\mathbf{x}^\star(t), \mathbf{u}^\star(t)) = \dot{\mathbf{x}}^\star(t)$. Here a denotes a constant rotor angular acceleration, such that the rotor speed increases ($a > 0$)

IEEE Robotics and Automation Letters (RA-L) paper, presented at ICRA 2026, Vienna, Austria. Cite as RA-L paper.

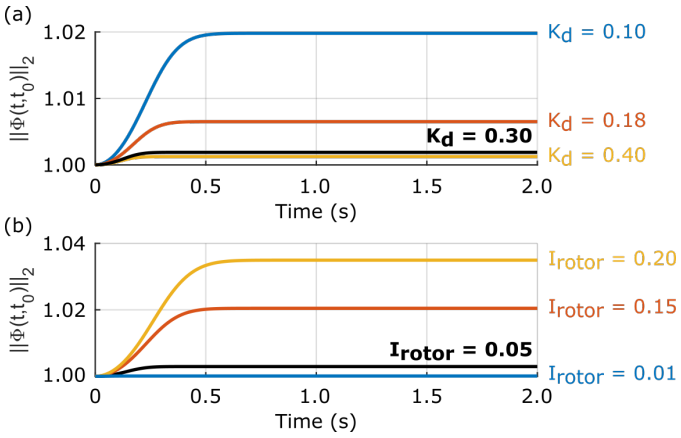

Fig. 3. State–transition norm $\|\Phi(t,t_0)\|_2$ along the constant-acceleration spin-up trajectory $x_1^\star(t) = at$. (a) Effect of rotor drag K_d with I_{rotor} fixed. (b) Effect of rotor inertia I_{rotor} with K_d fixed. The estimated $K_d = 0.30$ $\text{kg}\,\text{m}^2$ and $I_{\text{rotor}} = 0.05$ $\text{kg}\,\text{m}^2$ for the vehicle are plotted in black. Note that all parameters K_d and I_{rotor} have units $\text{kg}\,\text{m}^2$.

or decreases ($a < 0$) linearly with time. Linearization about this trajectory yields the linear time-varying (LTV) model $\delta\dot{\mathbf{x}}(t) = A(t)\,\delta\mathbf{x}(t) + B\,\delta\mathbf{u}(t)$, where $A(t)$ is time-varying and B is identical to the equilibrium case (Equation 6):

$$A(t) = \begin{bmatrix} -\frac{2K_d a t}{I_{\text{rotor}}} & 0 & 0 \\ 0 & 0 & 0 \\ -\frac{2K_\ell a t}{m} & 0 & 0 \end{bmatrix}.$$

Stability along this trajectory is evaluated by integrating the variational dynamics $\dot{\Phi}(t,t_0) = A(t)\Phi(t,t_0)$ with $\Phi(t_0,t_0) = I$, and monitoring the induced 2–norm $\|\Phi(t,t_0)\|_2$, which represents the maximum amplification of perturbations between t_0 and t. As shown in Fig. 3, $\|\Phi(t,t_0)\|_2$ remains near unity at approximately 1.0025 for $K_d = 0.3$ $\text{kg}\,\text{m}^2$ and $I_{\text{rotor}} = 0.05$ $\text{kg}\,\text{m}^2$. Thus, disturbances experience at most a 0.25% bounded amplification, rather than a sustained growth or decay, consistent with marginally stable modes in LTV dynamics. The level of amplification depends on choice of K_d and I_{rotor}, as evidenced by the change in $\|\Phi(t,t_0)\|_2$ shown in Fig. 3. Technical details of the computation are provided in Appendix A.

D. Limitations

Across Case I (rotor stopped), Case II (constant-speed rotor), and Case III (constant rotor acceleration), the analytical model predicts marginal stability (i.e, the dynamics remain bounded in open loop but do not exhibit asymptotic decay of perturbations). These results are obtained from a reduced-order, two-axis model that includes only yaw and altitude dynamics under assumptions of uncoupled forces and body symmetry. To overcome these simplifications, we next develop a full 6-DoF computational model.

IV. Computational Simscape Modeling

To complement the analytical framework, a multibody model was constructed in Simscape [26] with custom aerodynamic extensions specific to the SPERO configuration. The computational model provides (i) full 6-DoF outputs for the rigid-body vehicle, and (ii) a physics-based testbed that enables one-to-one benchmarking against experimental data.

Fig. 4 summarizes the model architecture. Each component is imported as a mesh with automatically assigned mass and inertia. Motors B1–B7 and servos S1–S3 (as defined in Fig. 2b) are implemented with driven revolute joints [25]: servo joints are position-controlled, while brushless motors are rate-controlled. Aerodynamic forces on the main rotor are

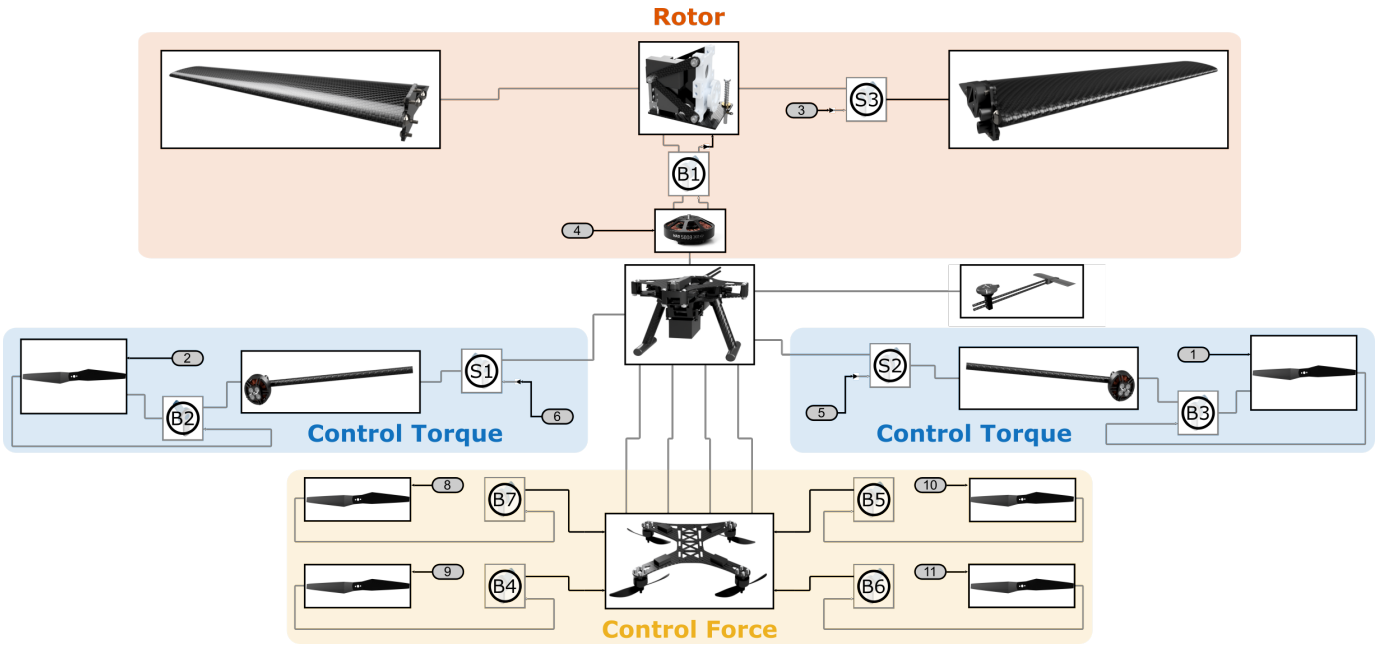

Fig. 4. Simscape multibody model of the SPERO [22] stop-rotor aircraft. The model incorporates the three actuation pathways: (orange) central rotor assembly with flipping wing (B1, S3), (blue) servo-vectored counterbalance motors (B2–B3 with servos S1–S2) generating control torque τ_u, and (yellow) base quadrotor motors (B4 – B7) providing control force F_u. Motor annotations (B1 – B7 and S1 – S3) overlay the revolute joint Simscape block [25]. Gray input blocks indicate actuator commands.

IEEE Robotics and Automation Letters (RA-L) paper, presented at ICRA 2026, Vienna, Austria. Cite as RA-L paper.

introduced through custom calculations. During VTOL, lift and drag are calculated from a tapered wing model [27]:

$$\mathrm{L,D} = \frac{1}{2}\rho c_{l,d}\omega_{\mathrm{rotor}}(t)^2\Big[\frac{m\left(r_{\mathrm{tip}}^4 - r_{\mathrm{root}}^4\right)}{4} + \frac{b\left(r_{\mathrm{tip}}^3 - r_{\mathrm{root}}^3\right)}{3}\Big],$$

where m and b are the coefficients defining the wing chord profile $c(l) = ml + b$ along the length l of the wing, and r_{tip} and r_{root} are the distances between the axis of rotation and the wing tip and root, respectively. In forward flight, the model uses standard lift and drag equations:

$$\mathrm{L,D} = \frac{1}{2}\rho c_{l,d} A_{\mathrm{ref}} v_x(t)^2,$$

where $v_x(t)$ is the forward translational velocity of the vehicle, as shown in Fig. 1. All forces are applied to through external force and torque blocks [28].

Control torque $\tau_u(t)$ is generated by two servo-vectored motors (blue blocks, B2–B3 with servos S1–S2), while supplemental control force $F_u(t)$ is produced by the quadrotor-style base motors (yellow blocks, B4 – B7). These actuation pathways directly map to the physical system and the analytical model (Table I). Model parameters are listed in Table II, and the full implementation is available online [29].

V. Model Validation and Experimental Benchmarking

The analytical and computational models are validated through two steps. First, analytical predictions are compared against the Simscape model to evaluate parity. Second, the computational model is benchmarked against restrained flight tests to evaluate correspondence with the physical system.

A. Simulation-Based Verification

Analytical models were validated through comparison with the Simscape model. During simulations, we constrained all degrees of freedom except the axis under investigation (i.e., yaw or vertical translation). A sigmoid function defined the rotor speed $\omega_{\mathrm{rotor}}(t)$ to ensure smooth, realistic accelerations, as plotted in Fig. 5(a). The simulated rotor speed exhibits marginal error from the commanded sigmoid function, with a maximum error of approximately 0.1% at maximum rotor acceleration (blue line, Fig. 5(a)). The simulation results (black line) are compared to the fitted analytical model (dashed red line) for yaw (Fig. 5(b)) and altitude (Fig. 5(c)). Simscape simulations employed the ode45 solver, which uses a Runge–Kutta method for non-stiff ordinary differential equations [31].

TABLE II
Simscape Simulation Parameters where α denotes angle of attack and Re denotes Reynolds number.

Parameter	Symbol	Value	Assumptions
Air Density	ρ	$1.225\,\mathrm{kg\,m^{-3}}$	Standard temperature and pressure
Lift Coefficient	c_l	0.75	NACA 0015; $\alpha = 7.5°$;
Drag Coefficient	c_d	0.04	$\mathrm{Re} = 5.0 \times 10^4$ [30]
Chord taper slope	m	-0.384	Root chord = 0.160 m; tip chord = 0.064 m
Chord taper offset	b	0.160 m	Same as root chord
Wing tip radius	r_{tip}	0.294 m	Distance between axis of rotation and wing tip
Wing root radius	r_{root}	0.047 m	Distance between axis of rotation and root
Wing reference area	A_{ref}	$0.056\,\mathrm{m^2}$	Wing span = 0.500 m

The analytical model results appear as colored data points in Fig. 5, where different colors and point sizes represent varying parameter values. For yaw dynamics, colors indicate different values of parameter $c_1 = \frac{I_{\mathrm{rotor}}}{I_{\mathrm{body}}}$, while point sizes correspond to parameter $c_2 = \frac{\rho c_d A_{\mathrm{ref}} r^3}{2 I_{\mathrm{body}}}$. For altitude dynamics, point colors represent different values of parameter $c_3 = \frac{\rho c_l A_{\mathrm{ref}} r^2}{2m}$. The parameters were calibrated through iterative manual tuning to visually align the analytical model to the simulated system response. The selected parameters ($c_1 = 1.15 \times 10^{-4}$, $c_2 = 8.00 \times 10^{-8}$, and $c_3 = 1.64 \times 10^{-4}$ m, summarized in Table III) generate the dashed red curves in Fig. 5(b) and Fig. 5(c) for yaw rate and altitude rate.

The parameter values c_1, c_2, and c_3 of the Simscape model are internally computed as a function of the geometry, material properties, and aerodynamic properties (Table II). The estimated parameter values for the Simscape simulation are summarized in Table III. The variation between the analytical

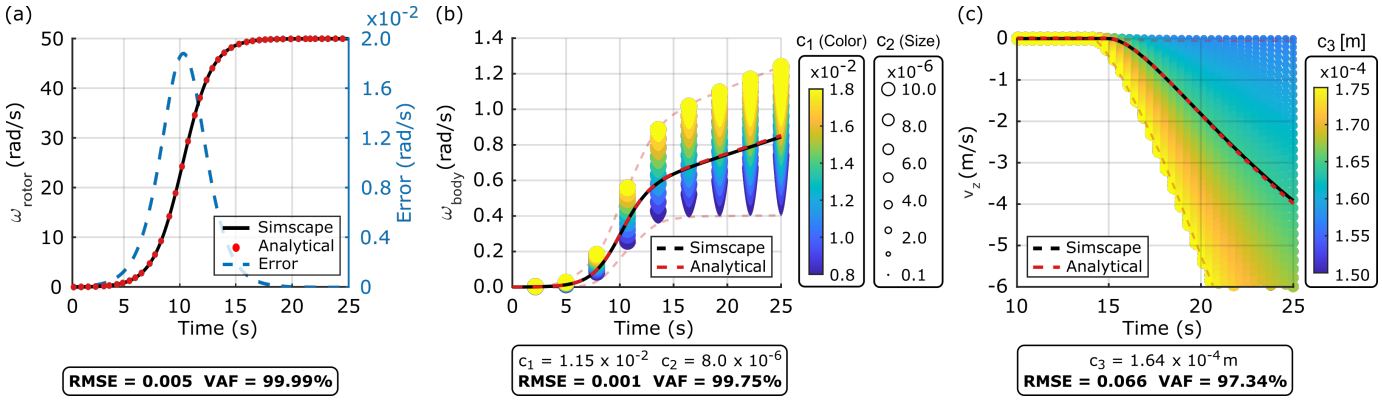

Fig. 5. Comparison of the analytical model (red) and full-state Simscape computational model (black) for(a) commanded rotor speed ω_{rotor}, (b) body yaw rate ω_{body}, and (c) vertical velocity v_z. The analytical model is computed over a range of constant parameters where $c_1 = \frac{I_{\mathrm{rotor}}}{I_{\mathrm{body}}}$, $c_2 = \frac{\rho c_d A_{\mathrm{ref}} r^3}{2 I_{\mathrm{body}}}$, and $c_3 = \frac{\rho c_l A_{\mathrm{ref}} r^2}{2m}$. The solution space is visualized using a color map for c_1 and c_3 and marker size for c_2. The faint red dashed line indicates the envelope of analytical values across the parameter ranges. The bright dashed red line corresponds to the analytical model evaluated at the fitted parameter values shown on the plot. Simulations were run for 70 s; the plots show the 15–40 s interval, re-indexed so that 15 s corresponds to 0 s on the time axis.

IEEE Robotics and Automation Letters (RA-L) paper, presented at ICRA 2026, Vienna, Austria. Cite as RA-L paper.

TABLE III
COMPARISON OF MODEL CONSTANTS. NOTE THAT c_1 AND c_2 ARE DIMENSIONLESS, WHILE c_3 HAS UNITS OF LENGTH

Parameter	Physical System	Analytical	Simscape
c_1	4.64×10^{-2}	1.15×10^{-2}	1.11×10^{-2}
c_2	4.97×10^{-5}	8.00×10^{-6}	2.62×10^{-5}
c_3 [m]	1.09×10^{-4}	1.64×10^{-4}	8.24×10^{-5}

and Simscape parameters, especially with c_2, suggest that the analytical coefficients act as effective lumped parameters that absorb differences in how aerodynamic forces and mass properties are represented in the Simscape model.

B. Experimental Benchmarking

The computational models were validated using constrained flight tests on a custom testing rig (Fig. 6) that permits rotational motion (i.e., roll, pitch, and yaw) while restricting translational motion. The rig consists of a t-slot aluminum frame supporting a rotating polyvinyl chloride (PVC) frame attached with two joint types:

1) **Plate-to-Frame Joints** (Fig. 6(a)) connect the rotating mechanism to the outer frame via a 3D-printed hub with a bearing. A bolt passes through the bearing into a t-slot frame nut, with a spacer offsetting the plates from the frame,
2) **Plate-to-Plate Joints** (Fig. 6(b)) connect the PVC sections along different rotation axes, where each PVC section mounts to a 3D-printed hub. The rotating hub contains a bearing through which a bolt threads into the opposing hub.

During experimental benchmarking, motor commands were supplied directly to the vehicle, and roll, pitch, yaw, and motor commands were recorded. The motor commands were then supplied to the computational model, which compensated for

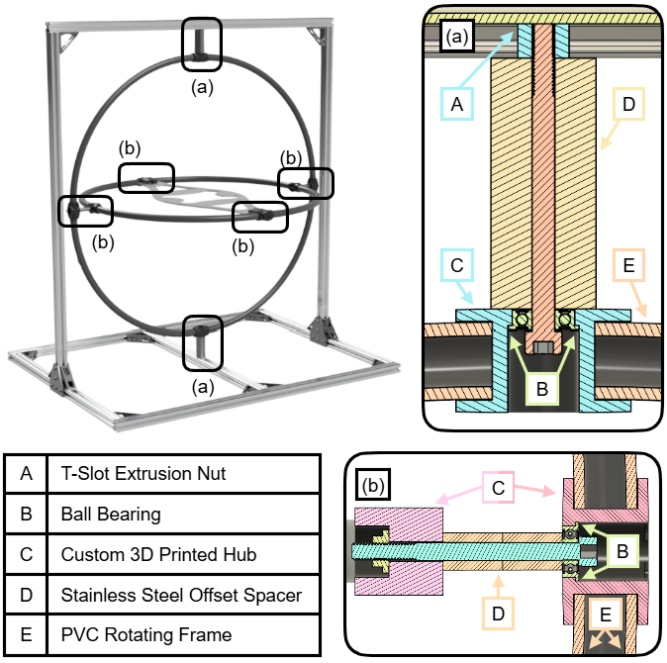

Fig. 6. Overview of the testing rig used for restrained flight tests including cross sections of the (a) plate-to-frame joint and (b) plate-to-plate joint.

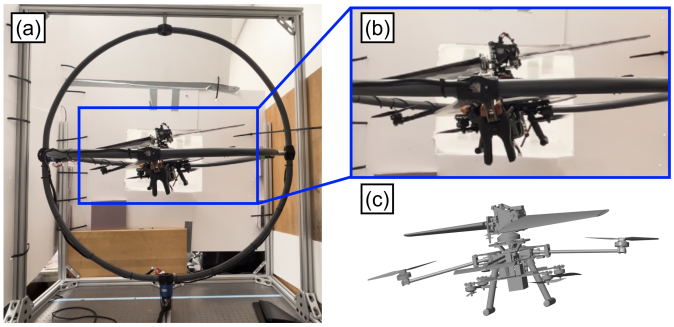

Fig. 7. Overview of the restrained flight test with (a) the vehicle mounted in the apparatus during the test, (b) a magnified view, and (c) the simulated vehicle at the same time instance.

rig inertia while constraining translational motion in x, y, and z.

Fig. 7 provides a qualitative comparison between the physical test (Fig. 7(a) with a magnified view in Fig. 7(b)) and the corresponding simulation frame (Fig. 7(c)). Quantitative comparisons between simulated (orange) and measured (blue) responses are presented in Fig. 8, with separate plots for roll (Fig. 8(a)), pitch (Fig. 8(b)), and yaw (Fig. 8(c)). While the simulated responses exhibit similar slopes to the measured values, the simulated values underestimate roll and yaw magnitudes while overestimating pitch magnitudes.

The baseline parameters used in these simulations ($D_x = 1.75$ Ns/m, $D_y = 3.75$ Ns/m, $D_z = 4.375$ Ns/m, $D_s = 0.075$ Ns/m, $CG_x = -2.54$ mm, $CG_y = 2.22$ mm, $CG_z = -152$ mm, $m = 2.42$ kg) were obtained by iterative tuning against constrained flight tests. Direct identification of absolute damping terms was not feasible due to the complexity of the rig system. Consequently, we selected $(D_x, D_y, D_z, D_s, CG_x, CG_y, CG_z, m)$ as the primary tuning variables and adjusted them through modifying the parameter values within the 6-DoF Simscape block until simulated roll, pitch, and yaw generated the measured trends. These tuned values then served as the center points for the perturbations used in the sensitivity study.

Fig. 8(d)–(f) summarizes the parameter sensitivity and reveals the following trend: spherical damping (D_s) influences the response across roll, pitch, and yaw, while CG location and mass emerge as secondary influences. This pattern indicates that discrepancies between simulated and measured responses are more effectively addressed by refining D_s and mass properties, rather than directional damping (D_x, D_y, D_z). More broadly, the analysis demonstrates how sensitivity metrics can be used not only to interpret current discrepancies but also to prioritize future measurements and parameter refinement. The raw data supporting this analysis are available online [32], and the coefficient-generation methodology is described in Appendix B.

VI. DISCUSSION

Model quality is quantified using variance accounted for (VAF), defined as:

$$\mathrm{VAF} = 1 - \frac{\mathrm{var}(y - f)}{\mathrm{var}(y)}, \tag{7}$$

IEEE Robotics and Automation Letters (RA-L) paper, presented at ICRA 2026, Vienna, Austria. Cite as RA-L paper.

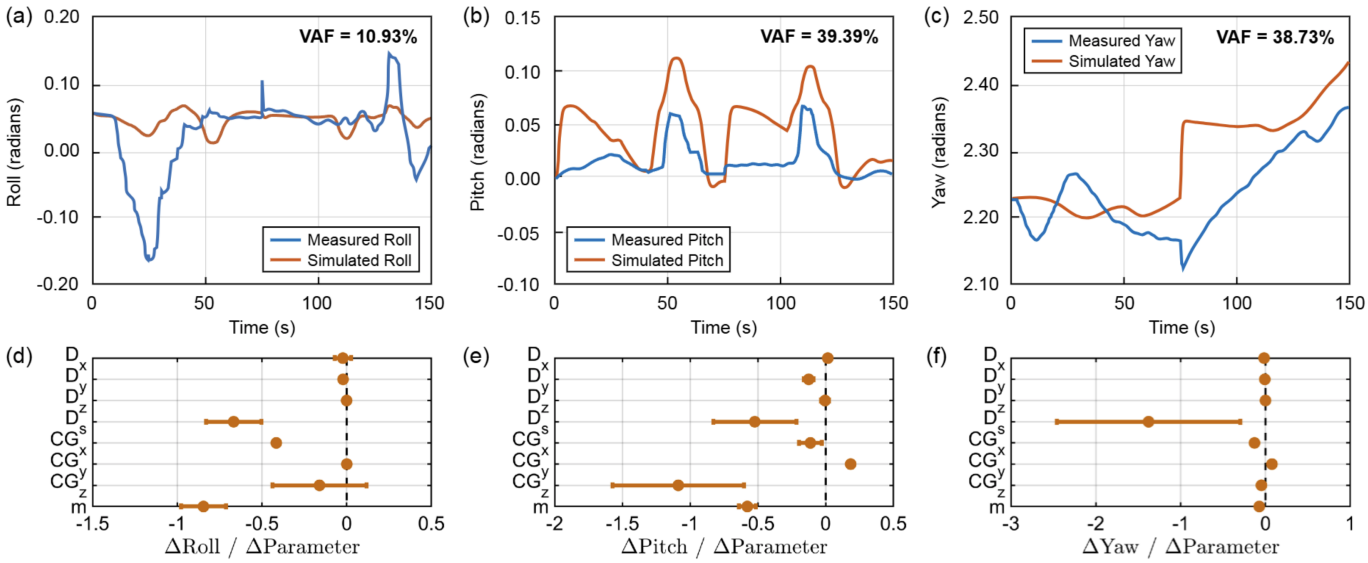

Fig. 8. Results from simulation of the computational model (orange) and constrained flight test data (blue) in (a) roll, (b) pitch, and (c) yaw. Panels (d)–(f) show the normalized sensitivity of each rotational degree of freedom to model parameters, including translational damping (D_x, D_y, D_z), spherical damping (D_s), center of gravity coordinates (CG_x, CG_y, CG_z), and mass (m). Sensitivity values represent the slope of a linear fit to the output as each parameter is perturbed. Error bars indicate 95% confidence bounds.

where y is the measured values, f is the predicted values, and $\mathrm{var}(x) = \frac{1}{n-1}\sum_{i=1}^{n}(x_i - \bar{x})^2$ is the variance of a data set x containing n data points with mean $\bar{x}$.

A. Analytical Model Quality

The analytical models (Section III) demonstrate strong agreement with the computational model, capturing 99.75% and 97.34% of the simulated yaw and altitude variance, respectively (Fig. 5), reflecting the shared foundations of the models in first-principles physics and simplified aerodynamics. This agreement validates that the analytical formulation captures the dominant effects along the yaw and altitude axes. At the same time, sensitivity analysis shows that model accuracy depends strongly on the coefficients c_1, c_2, and c_3, underscoring the need for careful parameter estimation when applying the model to physical systems.

B. Computational Model Quality

In contrast, the Simscape model (Section IV) reproduces qualitative trends from constrained flight tests (Fig. 8(a)–(c)) but shows quantitative discrepancies, with VAF values of 10.93%, 39.39%, and 38.73% for roll, pitch, and yaw, respectively. These lower values highlight the impact of unmodeled effects introduced by the physical rig and vehicle, such as viscous damping, joint friction, compliance, aerodynamic interactions, and parameter uncertainty, none of which are represented in the developed model. Improving the predictive performance of the computational model will require targeted parameter identification and incorporation of secondary physical effects.

VII. Conclusion

This paper presented a modeling framework for stop-rotor aircraft that combines first-principles analytical models, computational Simscape model, and experimental testing. The analytical model provided tractable equations for yaw and altitude dynamics and enabled open-loop stability analysis, while the computational model captured the full six-degree-of-freedom behavior of the vehicle. Comparisons showed strong agreement between the analytical and computational models, confirming that the dominant dynamics are well captured, and experimental benchmarking highlighted where unmodeled effects such as damping and center-of-gravity placement become important.

Together, these results provide both insight and practical tools: the analytical model offers intuition for stability, and the computational model serves as a testbed for design refinement. Future work will refine aerodynamic modeling, improve parameter estimation, and extend validation to unrestrained flight across the full operating envelope. Future efforts will also extend stability validation to free-flight experiments, thereby directly testing the theoretical predictions presented in this work. These efforts will address current limitations and advance the reliable deployment of stop-rotor aircraft in missions requiring efficient VTOL and forward-flight performance.

Appendix A: Computation of $\|\Phi(t, t_0)\|_2$

The state–transition matrix $\Phi(t, t_0)$ was obtained by integrating the variational dynamics $\dot{\Phi}(t, t_0) = A(t)\Phi(t, t_0)$ with $\Phi(t_0, t_0) = I$. For each parameter setting, $\Phi(t, t_0)$ was vectorized and integrated using `ode45` [31] with relative and absolute tolerances of 10^{-9}. The induced 2–norm $\|\Phi(t, t_0)\|_2$ was then computed as the largest singular value at uniformly spaced times.

Appendix B: Parameter Sensitivity

To generate the sensitivity coefficients shown in Fig. 8(d)–(f), we performed a local sensitivity analysis on the computational model. Each parameter of interest was perturbed independently across a range of absolute values while holding

IEEE Robotics and Automation Letters (RA-L) paper, presented at ICRA 2026, Vienna, Austria. Cite as RA-L paper.

TABLE IV
PARAMETER RANGES FOR SENSITIVITY ANALYSIS OF COMPUTATIONAL MODELS

Parameter	Symbol	Range	Units
Damping – X	D_x	$[0,\ 4]$	$\mathrm{N\,m^{-1}\,s}$
Damping – Y	D_y	$[0,\ 5]$	$\mathrm{N\,m^{-1}\,s}$
Damping – Z	D_z	$[0,\ 5]$	$\mathrm{N\,m^{-1}\,s}$
Spherical Damping	D_s	$[1.430,\ 34.380]$	$\mathrm{N\,m\,rad^{-1}\,s}$
CG – X	CG_x	$[-0.025,\ 0.025]$	m
CG – Y	CG_y	$[-0.038,\ 0.025]$	m
CG – Z	CG_z	$[-0.203,\ -0.050]$	m
Vehicle Mass	m	$[1.950,\ 2.535]$	kg

all other parameters constant. The specific perturbation ranges used for each parameter are summarized in Table IV. The perturbation ranges were chosen relative to the manually tuned (i.e., test and adjust value until results look similar) values that matches the constrained experimental flight data. Accordingly, the range for D_x was limited to $[0, 4]\ \mathrm{N\,m^{-1}\,s}$, which already spans more than twice its tuned value, whereas the ranges for D_y and D_z were extended to $[0, 5]\ \mathrm{N\,m^{-1}\,s}$ to provide a comparable relative span across baseline values.

For each parameter, we recorded the peak magnitude of the simulated roll, pitch, and yaw angles over a 70 s flight simulation. A first-order polynomial was fit to the relationship between the parameter values (independent variable) and the corresponding peak attitude magnitudes (dependent variable) using MATLAB's `fit(x, y, 'poly1')` function. The slope of the linear fit quantifies the local sensitivity of each attitude component to that parameter and is the value reported in Fig. 8(d)–(f). All simulations were deterministic, with no added noise or disturbances. Therefore, only a single trial was performed for each case. Both the parameter values and the output magnitudes were normalized by the baseline values used in the tuned model. The error bars shown in Fig. 8(d)–(f) represent the 95% confidence bounds on the fitted slope coefficient, as returned by the `fit` function in MATLAB. The raw (unnormalized) parameter perturbation data and simulated output values are provided in [32].

REFERENCES

[1] Y. Zhou, H. Zhao, and Y. Liu, "An evaluative review of the VTOL technologies for unmanned and manned aerial vehicles," *Computer Communications*, vol. 149, pp. 356–369, 2020. [Online]. Available: https://www.sciencedirect.com/science/article/pii/S014036641930996X

[2] J. J. Gertler, "V-22 Osprey Tilt-Rotor Aircraft: Background and Issues for Congress," Congressional Research Service, Tech. Rep., 3 2011.

[3] M. J. Lopez, C. S. Duffy, M. B. Tischler, and P. Ruckel, "Bell V-280 hover flight dynamics model validation and update with flight test data," in *Vertical Flight Society 77th Annual Forum*, 2021.

[4] F. Fonte, M. Favale, A. Rigo, and G. Quaranta, "Enhanced Gust Load Recovery For The AW609 Tiltrotor," in *45th European Rotorcraft Forum (ERF 2019)*, 2019, pp. 485–497. [Online]. Available: https://re.public.polimi.it/bitstream/11311/1111806/1/FONTF02-19.pdf

[5] National Air and Space Museum, "Vertol VZ-2 (Model 76)." [Online]. Available: https://airandspace.si.edu/collection-objects/vertol-vz-2-model-76/nasm_A19650279000

[6] J. Nichols, "The Hiller X-18 Experimental Aircraft - Lessons Learned," in *Aircraft Design, Systems and Operations Conference*. Dayton, OH, USA: American Institute of Aeronautics and Astronautics, 1990.

[7] J. Konrad, "Flight and Operational Suitability Testing of the XC-142, V/STOL Assault Transport," in *Flight Test, Simulation and Support Conference*. Cocoa Beach, FL: American Institute of Aeronautics and Astronautics, 1967.

[8] Q. Quan, *Introduction to multicopter design and control*, 1st ed. Springer Singapore, 2017.

[9] N. B. Knoebel, S. R. Osborne, D. O. Snyder, T. W. McLain, R. W. Beard, and A. M. Eldredge, "Preliminary modeling, control, and trajectory design for miniature autonomous tailsitters," in *AIAA Guidance, Navigation, and Control Conference and Exhibit*. American Institute of Aeronautics and Astronautics, 2006.

[10] D. J. Taylor, M. V. Ol, and T. Cord, "SkyTote: An unmanned precision cargo delivery system," in *AIAA International Air and Space Symposium and Exposition: The Next 100 Years*. Dayton, OH, USA: American Institute of Aeronautics and Astronautics, 7 2003.

[11] Y. Ito, M. Hayashida, and H. Yasuda, "Concept of a logistics, air launch, and recovery (Lalar) evtol platform to support small-sized space vehicles," in *AIAA Aviation 2019 Forum*. Dallas, TX, USA: American Institute of Aeronautics and Astronautics, 6 2019.

[12] D. F. Finger, C. Braun, and C. Bil, "A Review of Configuration Design for Distributed Propulsion Transitioning VTOL Aircraft," *Asia-Pacific International Symposium on Aerospace Technology-APISAT*, pp. 3–5, 2017.

[13] G. E. Welch, "Assessment of aerodynamic challenges of a variable-speed power turbine for large civil tilt-rotor application," in *66th Annual Forum and Technology Display (AHS Forum 66)*. Phoenix, AZ, USA: National Aeronautics and Space Administration, 5 2010.

[14] A. Bacchini and E. Cestino, "Electric VTOL configurations comparison," *Aerospace*, vol. 6, no. 3, 2019.

[15] K. Hilby, "Design and Control of a Stop-Rotor Aircraft Enabled by Morphing Wings," Ph.D. dissertation, Massachusetts Institute of Technology, Cambridge, MA, 2 2025.

[16] G. E. Brown and V. Ahuja, "The Stopped Rotor Concept – A New Look At An Old Idea," in *AIAA Aviation 2023 Forum*. San Diego, CA, USA: American Institute of Aeronautics and Astronautics, 6 2023. [Online]. Available: https://arc.aiaa.org/doi/10.2514/6.2023-4388

[17] L. Young, "Novel Conceptual Designs for Stopped-Rotor Aerial Vehicles and Other High-Speed Rotorcraft," in *6th Decennial VFS Aeromechanics Specialists' Conference*, 2 2024.

[18] R. Guertin, "Development status of the RSRA/X-Wing," in *AIAA/AHS/ASEE Aircraft Design Systems and Operations Meeting*. Colorado Springs, CO, USA: American Institute of Aeronautics and Astronautics (AIAA), 10 1985.

[19] S. K. Tayman, "Stop-rotor rotary wing aircraft," US Patent 8,070,090, 12 2011.

[20] J. Bevirt, E. Stilson, A. Stoll, and P. Sinha, "Aerodynamically efficient lightweight vertical take-off and landing aircraft with multi-configuration wing tip mounted rotors," US Patent 10,035,587, 12 2018.

[21] P. Sinha, A. M. Stoll, E. V. Stilson, and J. Bevirt, "Design and testing of the Joby lotus multifunctional rotor VTOL UAV," in *15th AIAA Aviation Technology, Integration, and Operations Conference*. American Institute of Aeronautics and Astronautics, 2015.

[22] K. Hilby and I. Hunter, "Unlocking Stopped-Rotor Flight: Development and Validation of SPERO, a Novel UAV Platform," *arXiv preprint arXiv:2509.07812*, 2025.

[23] A. Vargas-Clara and S. Redkar, "Dynamics and Control of a Stop Rotor Unmanned Aerial Vehicle," *International Journal of Electrical and Computer Engineering*, vol. 2, no. 5, 10 2012.

[24] A. He, H. Gao, S. Zhang, Z. Gao, B. Ma, L. Chen, and W. Dai, "Full mode flight dynamics modelling and control of stopped-rotor UAV," *Chinese Journal of Aeronautics*, vol. 35, no. 10, 2022.

[25] MathWorks, "Revolute Joint." [Online]. Available: https://www.mathworks.com/help/sm/ref/revolutejoint.html

[26] ——, "Simscape Multibody." [Online]. Available: https://www.mathworks.com/products/simscape-multibody.html

[27] T. Kraeutner, "The Airfoil Method for Rotary Wing Analysis Using Modified Lift and Drag Equations," Department of Defense, Tech. Rep., 2021.

[28] Mathworks, "External Force and Torque." [Online]. Available: https://www.mathworks.com/help/sm/ref/externalforceandtorque.html

[29] K. Hilby, "Stop Rotor Simscape Model," 2025. [Online]. Available: https://github.com/kristanhilby/Stop-Rotor-Simscape-Model/

[30] M. Selig, "NACA 0015 (naca0015-il)." [Online]. Available: http://airfoiltools.com/airfoil/details?airfoil=naca0015-il

[31] Mathworks, "ode45." [Online]. Available: https://www.mathworks.com/help/matlab/ref/ode45.html

[32] K. Hilby, "Supporting Data for Stop-Rotor Model Validation." [Online]. Available: https://github.com/kristanhilby/stoprotor-modeling-dataset/